6th European Conference on Computational Mechanics (ECCM 6)
7th European Conference on Computational Fluid Dynamics (ECFD 7)
1115 June 2018, Glasgow, UK

MIXED FINITE ELEMENT FORMULATIONS FOR THE GALERKIN-BASED TIME INTEGRATION OF FINITE ANISOTROPIC ELASTODYNAMICS

Julian Dietzsch[1] **and Michael Groß**[2]

[1] Technische Universität Chemnitz, Professorship of applied mechanics and dynamics
Reichenhainer Straße 70, D-09126 Chemnitz, julian.dietzsch@mb.tu-chemnitz.de

[2] michael.gross@mb.tu-chemnitz.de

Key words: finite element method, locking, nearly incompressible elasticity, mixed finite elements, anisotropy

Abstract. Our research is motivated by dynamic simulations of fiber-reinforced materials in light-weight structures. For the description of the material behavior we use a hyperelastic, transversely isotropic and polyconvex formulation. On the one hand side we want to reduce the volumetric locking effect of the matrix part. Here we use well known mixed element formulations like the Displacment-Pressure formulation presented in [1], or the so called CoFEM element shown in [4]. Also we want to reduce the locking effect of the very stiff fiber as well. In [6] is shown a new efficient mixed element formulation, called SKA element. On the other hand side, we want to perform long-term simulations and require accurate high-order time integrators. We use an galerkin integrator with higer-order finite elements in time [5]. To obtain a solution we combine both, mixed finite elements and the Galerkin time integrator, to reduce the locking effects and reach a high accuracy. We compare the new elements with standard methods for hexahedral elements up to a cubic approximation in space. As numerical example serves the well-known cooks cantilever beam [4]. The Dirichlet boundary conditions are modeled by using Lagrange multipliers and as Neumann boundary condition a pressure distribution is used.

1 INTRODUCTION

Looking-free finite elements and energy-momentum schemes are two of the best-known improvements of finite element methods. Both are strongly marked by Professor Juan Carlos Simo (1952–1994).

The idea of using a Hu-Washizu functional for avoiding volumetric locking goes back at least to Reference [1]. In this reference, the determinand $\det\boldsymbol{F}$ of the deformation gradient $\boldsymbol{F}$ is introduced as independent field. In Reference [4], this idea is developed further by introducing a new mixed finite element based on different approximations of the minors of the deformation gradient. This method is further improved by the authors of Reference [6] for anisotropic nonlinear continua based on structural tensors.

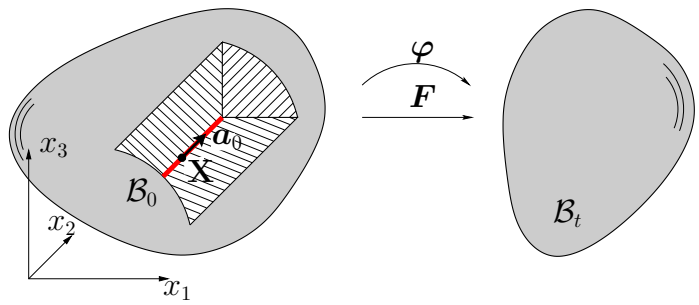

Figure 1: Undeformed configuration $\mathcal{B}_0$ with fiber direction $\mathbf{a}_0$ and deformed configuration $\mathcal{B}_t$ ($\boldsymbol{F}$ - Deformation gradient)

The starting point for strongly developing second-order accurate energy-momentum schemes is set by Reference [2]. Here, the focus is set on hyperelastic materials, especially on the St. Venant-Kirchhoff material model. In Reference [3], energy-momentum schemes are extended to algebraic constraints arising from the coupling between rigid and continuous bodies. The treatment of anisotropic nonlinear continua defined by structural tensors are the basis of Reference [5], wherein also the accuracy order of the energy-momentum schemes is extendend to $2\,k$ ($k = 1, 2, \ldots$).

The combination of both algorithmic improvements seems to be natural, in order to get more accurate results in dynamic simulations. Therefore, in Reference [8], finite elements based on the classical scaling of the deformation gradient with an assumed Jacobian (compare Reference [1]), is realized within a second-order accurate energy-momentum scheme. The combination of energy-momentum schemes based on Hamilton's principle and higher-order finite elements in space is currently published in Reference [7] in an efficient way. Further, the combination of locking-free finite elements based on a polyconvex material formulation (compare Reference [4]) is shown in Reference [9].

In the present paper, we show first numerical results of the combination of higher-order Galerkin-based schemes and different mixed finite element based space approximations. Here, we also treat anisotropic nonlinear continua based on structural tensors. In the framework of dynamic simulations, we could further improved the finite element formulation presented in Reference [6]. This is shown by many convergence studies with the well-known cook's membrane problem, which also considered in References [4, 9].

2 FINITE ELEMENT FORMULATION

As continuum model, we consider a transversely isotropic material with fiber direction $\mathbf{a}_0$ (see Figure 1). With the the structural tensor $\boldsymbol{M} = \boldsymbol{a}_0 \otimes \boldsymbol{a}_0$ and the right Cauchy-Green tensor $\boldsymbol{C} = \boldsymbol{F}^T\boldsymbol{F}$ we define the fourth $I_4(\boldsymbol{C}) = \mathrm{tr}[\boldsymbol{C}\boldsymbol{M}]$ and fifth $I_5(\boldsymbol{C}) = \mathrm{tr}[\mathrm{cof}[\boldsymbol{C}\boldsymbol{M}]]$ invariant. We split the strain energy function into an isotropic function Ψ^{iso} and an transversely isotropic part Ψ^{ti} ($J = \det[\boldsymbol{F}] = \sqrt{\det[\boldsymbol{C}]}$). Therefore, we obtain

$$\Psi(\boldsymbol{C}, \boldsymbol{M}) = \Psi^{iso}(\boldsymbol{C}, \mathrm{cof}[\boldsymbol{C}], J) + \Psi^{ti}(\boldsymbol{C}, \mathrm{cof}[\boldsymbol{C}], J, \boldsymbol{M}) \tag{1}$$

$$= \Psi^{iso}(\boldsymbol{C}, \mathrm{cof}[\boldsymbol{C}], J) + \Psi^{ti}(I_4(\boldsymbol{C}), I_5(\boldsymbol{C}), J) \tag{2}$$

The considered finite element discretizations in space are based on Hu-Washizu functionals. As point of departure, we consider the functional corresponding to the standard displacement element, given by

$$\Pi^{D}_{HW}(\boldsymbol{q}) = \int_{\mathcal{B}_0} \Psi(\boldsymbol{C}(\boldsymbol{q}))\mathrm{d}V \tag{3}$$

The second one leads to the well known displacement-pressure element introduced by Simo et al. in [1], with the independent variable for volumetric dilatation Θ and the corresponding Lagrange multiplier p wich plays the role of the hydrostatic pressure.

$$\Pi^{DP}_{HW}(\boldsymbol{q}, \Theta, p) = \Pi^{D}_{HW} + \int_{\mathcal{B}_0} p(J(\boldsymbol{q}) - \Theta)\mathrm{d}V \tag{4}$$

with $\Psi(\boldsymbol{C}, \Theta, \boldsymbol{M}) = \Psi^{iso}(\boldsymbol{C}, \mathrm{cof}[\boldsymbol{C}], \Theta) + \Psi^{ti}(\boldsymbol{C}, \mathrm{cof}[\boldsymbol{C}], \Theta, \boldsymbol{M})$. By adding further fields for the cofactor of $\boldsymbol{C}$ we obtain a third functional as shown in [4]:

$$\Pi^{CoFEM}_{HW}(\boldsymbol{q}, \ldots, \boldsymbol{H}_{\mathrm{cof}[\boldsymbol{C}]}, \boldsymbol{B}_{\mathrm{cof}[\boldsymbol{C}]}) = \Pi^{DP}_{HW} + \int_{\mathcal{B}_0} \boldsymbol{B}_{\mathrm{cof}[\boldsymbol{C}]} : (\mathrm{cof}[\boldsymbol{C}(\boldsymbol{q})] - \boldsymbol{H}_{\mathrm{cof}[\boldsymbol{C}]})\mathrm{d}V \tag{5}$$

with $\Psi(\boldsymbol{C}, \boldsymbol{H}_{\mathrm{cof}[\boldsymbol{C}]}, \Theta, \boldsymbol{M}) = \Psi^{iso}(\boldsymbol{C}, \boldsymbol{H}_{\mathrm{cof}[\boldsymbol{C}]}, \Theta) + \Psi^{ti}(\boldsymbol{C}, \boldsymbol{H}_{\mathrm{cof}[\boldsymbol{C}]}, \Theta, \boldsymbol{M})$. An other element, especially for anisotropic material formulations, is shown in [6]. In this element formulation (called SKA element) an additional field $\boldsymbol{C}_A$ is introduced. The corresponding Lagrange multiplier $\boldsymbol{S}_A$ represent the part of the stress tensor which is caused by the anisotropic part of the material formulation Ψ^{ti}. Here, we arrive at

$$\Pi^{CoSKA}_{HW}(\boldsymbol{q}, \ldots, \boldsymbol{C}_A, \boldsymbol{S}_A) = \Pi^{CoFEM}_{HW} + \int_{\mathcal{B}_0} \frac{1}{2}\boldsymbol{S}_A(\boldsymbol{C} - \boldsymbol{C}_A)\mathrm{d}V \tag{6}$$

with $\Psi(\boldsymbol{C}, \boldsymbol{H}_{\mathrm{cof}[\boldsymbol{C}]}, \Theta, \boldsymbol{C}_A, \boldsymbol{M}) = \Psi^{iso}(\boldsymbol{C}, \boldsymbol{H}_{\mathrm{cof}[\boldsymbol{C}]}, \Theta) + \Psi^{ti}(\boldsymbol{C}_A, \mathrm{cof}[\boldsymbol{C}_A], \sqrt{\det[\boldsymbol{C}_A]}, \boldsymbol{M})$. On top of that we propose a formulation (CoCoA element) with the additional fields $\boldsymbol{H}_{\mathrm{cof}[\boldsymbol{C}_A]}$ and Θ_A and the corresponding Lagrange multipliers $\boldsymbol{B}_{\mathrm{cof}[\boldsymbol{C}_A]}$ and p_A, given by

$$\begin{aligned}
&\Pi^{CoCoA}_{HW}(\boldsymbol{q}, \ldots, \boldsymbol{H}_{\mathrm{cof}[\boldsymbol{C}_A]}, \boldsymbol{B}_{\mathrm{cof}[\boldsymbol{C}_A]}, \Theta_A, p_A) \\
&= \Pi^{CoSKA}_{HW} + \int_{\mathcal{B}_0} \boldsymbol{B}_{\mathrm{cof}[\boldsymbol{C}_A]} : (\mathrm{cof}[\boldsymbol{C}(\boldsymbol{q})] - \boldsymbol{H}_{\mathrm{cof}[\boldsymbol{C}_A]})\mathrm{d}V + \int_{\mathcal{B}_0} p_A(J - \Theta_A)\mathrm{d}V
\end{aligned} \tag{7}$$

with $\Psi(\ldots, \boldsymbol{C}_A, \boldsymbol{H}_{\mathrm{cof}[\boldsymbol{C}_A]}, \Theta_A, \boldsymbol{M}) = \Psi^{iso}(\ldots) + \Psi^{ti}(\boldsymbol{C}_A, \boldsymbol{H}_{\mathrm{cof}[\boldsymbol{C}_A]}, \Theta_A, \boldsymbol{M})$. This element can also be reformulated in the two invariants $I_4(\boldsymbol{C})$ and $I_5(\boldsymbol{C})$, so that

$$\begin{aligned}
\Pi^{CoA}_{HW}(\boldsymbol{q}, \ldots, h_{I_4}, b_{I_4}, h_{I_5}, b_{I_5}) = \Pi^{CoFEM}_{HW} &+ \int_{\mathcal{B}_0} b_{I_4}(I_4(\boldsymbol{C}) - h_{I_4})\mathrm{d}V \\
&+ \int_{\mathcal{B}_0} b_{I_5}(I_5(\boldsymbol{C}) - h_{I_5})\mathrm{d}V + \int_{\mathcal{B}_0} p_A(J - \Theta_A)\mathrm{d}V
\end{aligned} \tag{8}$$

with $\Psi(\boldsymbol{C}, \boldsymbol{H}_{\mathrm{cof}[\boldsymbol{C}]}, \Theta, h_{I_4}, h_{I_5}, \Theta_A) = \Psi^{iso}(\boldsymbol{C}, \boldsymbol{H}_{\mathrm{cof}[\boldsymbol{C}]}, \Theta) + \Psi^{ti}(h_{I_4}, h_{I_5}, \Theta_A)$. For dynamic problems we have to consider kinetic energy and a mixed functional term with linear

momentum $\boldsymbol{p}$ and velocity $\boldsymbol{v}$ to get a Hamiltonian formulation, which leads to a Veubeke-Hu-Washizu functional.

$$\Pi_{VHW}(\boldsymbol{q},\dot{\boldsymbol{q}},\boldsymbol{v},\boldsymbol{p},\dots) = \int_T\int_{\mathcal{B}_0}\frac{1}{2}\rho_0\boldsymbol{v}^T\boldsymbol{v}\mathrm{d}V\mathrm{d}t + \int_T\int_{\mathcal{B}_0}\boldsymbol{p}(\dot{\boldsymbol{q}}-\boldsymbol{v})\mathrm{d}V\mathrm{d}t - \int_T\Pi_{HW}(\boldsymbol{q},\dots)\mathrm{d}t + \int_T\int_{\partial\mathcal{B}_0}\boldsymbol{t}\cdot\boldsymbol{q}\mathrm{d}A\mathrm{d}t + \int_{\partial\mathcal{B}_0}\boldsymbol{\lambda}[\boldsymbol{q}-\boldsymbol{q}^{\mathrm{ref}}]\mathrm{d}A \tag{9}$$

Dirichlet boundary conditions are modelled by Lagrange multipliers $\boldsymbol{\lambda}$ as shown in [3], and $\boldsymbol{t}$ denotes the boundary traction vector for the Neumann boundary conditions. By variation with respect to all unknowns we obtain the weak forms. As an example we show the weak forms of the CoCoA element, given by

$$\begin{aligned}
&\int_T\int_{\mathcal{B}_0}(\mathrm{div}[\boldsymbol{F}\boldsymbol{S}]-\dot{\boldsymbol{p}})\delta\boldsymbol{q}\mathrm{d}V\mathrm{d}t = 0 && \int_T\int_{\mathcal{B}_0}(\frac{1}{\rho_0}\boldsymbol{p}-\dot{\boldsymbol{q}})\delta\boldsymbol{p}\mathrm{d}V\mathrm{d}t = 0\\
&\int_T\int_{\mathcal{B}_0}\frac{1}{2}(\boldsymbol{C}_A-\boldsymbol{C})\delta\boldsymbol{S}_A\mathrm{d}V\mathrm{d}t = 0 && \int_T\int_{\mathcal{B}_0}(\frac{1}{2}\boldsymbol{S}_A-\frac{\partial\Psi}{\partial\boldsymbol{C}_A})\delta\boldsymbol{C}_A\mathrm{d}V\mathrm{d}t = 0\\
&\int_T\int_{\mathcal{B}_0}(\Theta-J)\delta p\mathrm{d}V\mathrm{d}t = 0 && \int_T\int_{\mathcal{B}_0}(\boldsymbol{H}_{\mathrm{cof}[\boldsymbol{C}]}-\mathrm{cof}[\boldsymbol{C}])\delta\boldsymbol{B}_{\mathrm{cof}[\boldsymbol{C}]}\mathrm{d}V\mathrm{d}t = 0\\
&\int_T\int_{\mathcal{B}_0}(p-\frac{\partial\Psi}{\partial\Theta})\delta\Theta\mathrm{d}V\mathrm{d}t = 0 && \int_T\int_{\mathcal{B}_0}(\boldsymbol{B}_{\mathrm{cof}[\boldsymbol{C}]}-\frac{\partial\Psi}{\partial\boldsymbol{H}_{\mathrm{cof}[\boldsymbol{C}]}})\delta\boldsymbol{H}_{\mathrm{cof}[\boldsymbol{C}]}\mathrm{d}V\mathrm{d}t = 0\\
&\int_T\int_{\mathcal{B}_0}(\Theta_A-J)\delta p_A\mathrm{d}V\mathrm{d}t = 0 && \int_T\int_{\mathcal{B}_0}(\boldsymbol{H}_{\mathrm{cof}[\boldsymbol{C}_A]}-\mathrm{cof}[\boldsymbol{C}])\delta\boldsymbol{B}_{\mathrm{cof}[\boldsymbol{C}_A]}\mathrm{d}V\mathrm{d}t = 0\\
&\int_T\int_{\mathcal{B}_0}(p_A-\frac{\partial\Psi}{\partial\Theta_A})\delta\Theta_A\mathrm{d}V\mathrm{d}t = 0 && \int_T\int_{\mathcal{B}_0}(\boldsymbol{B}_{\mathrm{cof}[\boldsymbol{C}_A]}-\frac{\partial\Psi}{\partial\boldsymbol{H}_{\mathrm{cof}[\boldsymbol{C}_A]}})\delta\boldsymbol{H}_{\mathrm{cof}[\boldsymbol{C}_A]}\mathrm{d}V\mathrm{d}t = 0
\end{aligned}$$

where $\boldsymbol{S} = (2\frac{\partial\Psi}{\partial\boldsymbol{C}} + 2\boldsymbol{B}_{\mathrm{cof}[\boldsymbol{C}]} : \mathbb{P} + pJ^{-1}\mathrm{cof}[\boldsymbol{C}] + \boldsymbol{S}_A + 2\boldsymbol{B}_{\mathrm{cof}[\boldsymbol{C}_A]} : \mathbb{P} + p_AJ^{-1}\mathrm{cof}[\boldsymbol{C}])$ and $\mathbb{P} = \frac{\partial\mathrm{cof}[\boldsymbol{C}]}{\partial\boldsymbol{C}}$. All quantities are approximated with Lagrangian shape functions in space (see Reference [7]) and time (see Reference [5]). All exsisting integrals are solved with the corresponding Gaussian quadrature rule. Finally we eliminate $\boldsymbol{p}$ and condense out the obtained formulation at the element level to a pure displacement formulation (see Reference [4]). Hence, all mixed fields beside $\boldsymbol{q}$ are discontinuous at the boundaries of spatial elements.

3 NUMERICAL EXAMPLES

As numerical example serves the well-known Cook's cantilever beam with a quadratic distribution of an in-plane load on the Neumann boundary with the prescribed simulation parameters shown in Figure 2. The strain energy function for isotropic and transversely

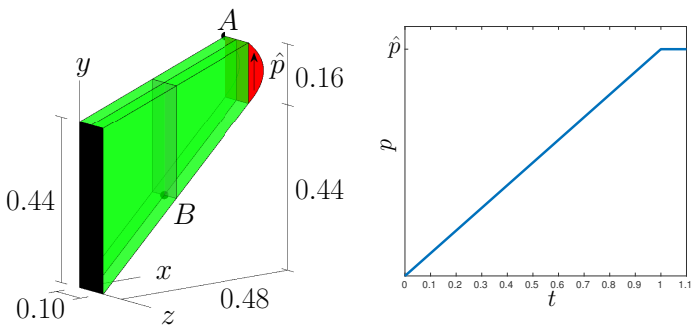

$\epsilon_1 = 16e6$	$\epsilon_8 = 8$
$\epsilon_2 = 32e6$	$\epsilon_9 = 1$
$\epsilon_3 = 480e6$	$\rho_0 = 1000$
$\epsilon_4 = 80e6$	$T = 1.1$
$\epsilon_5 = 20$	$h_n = 0.005$
$\epsilon_6 = 1200e6$	$TOL = 1e-5$
$\epsilon_7 = 4$	$\hat{p} = 4.9e8$

Figure 2: Geometry of Cook's cantilever beam (left), and the prescribed simulation parameters (right)

isotropic part is given by

$$\Psi^{iso}(\boldsymbol{C}) = \frac{\epsilon_1}{2}(\mathrm{tr}[\boldsymbol{C}])^2 + \frac{\epsilon_2}{2}(\mathrm{tr}[\mathrm{cof}[\boldsymbol{C}]])^2 - \epsilon_3 \ln(\sqrt{J}) + \frac{\epsilon_4}{2}(J^{\epsilon_5} + J^{-\epsilon_5} - 2)$$
$$\Psi^{ti}(\boldsymbol{C}) = \epsilon_6 \left(\frac{1}{\epsilon_7 + 1}(\mathrm{tr}[\boldsymbol{C}\boldsymbol{M}])^{\epsilon_7+1} + \frac{1}{\epsilon_8 + 1}(\mathrm{tr}[\mathrm{cof}[\boldsymbol{C}]\boldsymbol{M}])^{\epsilon_8+1} + \frac{1}{\epsilon_9}\det[\boldsymbol{C}]^{-\epsilon_9} \right)$$

which are shown in Reference [4]. The used fiber direction is $\mathbf{a}_0^T = [1\ 1\ 1]$. We compare the proposed mixed finite elements (CoA and CoCoA) and the non-standard mixed elements (CoSKA and CoFEM) with the standard displacement element and displacement-pressure element for hexahedral elements up to cubic order. Herein, we analyze the spatial convergence for various combinations of polynomial degrees in space of the independent quantities. The element title starts with H for a linear hexahedral element or HS for a quadtratic/cubic serendipity hexahedral element. This is followed by the element type and the information about the polynomial degrees of all quantities (see Table 1).

digit nr.:	1	2	3	4	5	6
pol. degree of:	$\boldsymbol{q}$	$\boldsymbol{H}_{\mathrm{cof}[\boldsymbol{C}]}$,$\boldsymbol{B}_{\mathrm{cof}[\boldsymbol{C}]}$	Θ,p	$\boldsymbol{C}_A$,$\boldsymbol{S}_A$	$\boldsymbol{H}_{\mathrm{cof}[\boldsymbol{C}_A]}$,$\boldsymbol{B}_{\mathrm{cof}[\boldsymbol{C}_A]}$	Θ_A,p_A

Table 1: Numbering of the polynomial degrees.

Table 2 shows the convergence of the y-coordinate of all calculated elements. Red lines mean that the calculation is not converged. Figure 3 shows an selection of the elements and Figure 4 the same selection for the stress σ_{xx}. The CoA element and CoCoA element provide equal solutions. CoCoA elements with a low polynomial degree for the quantities of Ψ^{ti} have the highest convergence rate, followed by the CoFEM elements. The worst solution produce the linear standard elements. Many of the high order CoSKA elements do not converge. In the case of linear approximation, the HCoCoA100000 element show an fast convergence and is within the range of the HS2 standard element. The HCoSKA1000 element have an even higher convergence rate, but it shows an hourglass effect. This is demonstrat in Figure 5. Here, various elements are displayed and we can see hourglass modes at the HCoSKA1000 and HCoSKA2100 element. This could also be the reason why many of the CoSKA elements do not converge.

n_{el} =	32	256	864	2048	6912	35301
n_{dof} =	225	1215	3549	7803	24375	105903
H1	0.7071	0.7464	0.7659	0.7760	0.7853	0.7915
HDP10	0.7264	0.7642	0.7783	0.7848	0.7903	0.7940
HCo100	0.7752	0.7905	0.7937	0.7950	0.7960	0.7967
HCoSKA1000	0.7923	0.7951	0.7961	0.7966	0.7970	0.7973
HCoA100000	0.7760	0.7907	0.7939	0.7951	0.7961	0.7968
HCoSCoA100000	0.7760	0.7907	0.7939	0.7951	0.7961	0.7968

n_{el} =	32	256	864	2048	4000	6912
n_{dof} =	735	4347	13143	29427	55503	93675
HS2	0.7896	0.7946	0.7958	0.7962	0.7965	0.7967
HSDP20	0.7921	0.7957	0.7965	0.7968	0.7970	0.7971
HSCo200	0.7958	0.7969	0.7972	0.7974	0.7974	0.7975
HSCo210	0.7928	0.7959	0.7966	0.7969	0.7971	0.7972
HSCoSKA2100	0.8017	0.8008	0.8000	0.7996	0.7150	0.7920
HSCoSKA2101	0.7918	0.7951	0.7961	0.7966	0.7968	0.7970
HSCoSKA2000	0.7835	0.7227	0.7136	0.7020	0.6986	0.6967
HSCoSKA2001	0.7919	0.7951	0.7961	0.7966	0.7968	0.7970
HSCoA210000	0.7969	0.7973	0.7975	0.7976	0.7976	0.7977
HSCoA210100	0.7956	0.7969	0.7972	0.7973	0.7974	0.7975
HSCoA200000	0.7975	0.7974	0.7976	0.7976	0.7977	0.7977
HSCoA200100	0.7959	0.7970	0.7973	0.7974	0.7975	0.7975
HSCoCoA210000	0.7969	0.7973	0.7975	0.7976	0.7976	0.7977
HSCoCoA210100	0.7956	0.7969	0.7972	0.7973	0.7974	0.7975
HSCoCoA200000	0.7975	0.7974	0.7976	0.7976	0.7977	0.7977
HSCoCoA200100	0.7959	0.7970	0.7973	0.7974	0.7975	0.7975

n_{el} =	32	256	864	2048	4000
n_{dof} =	1245	7479	22737	51051	96453
HS3	0.7915	0.7951	0.7961	0.7965	0.7968
HSDP30	0.7931	0.7961	0.7968	0.7971	0.7972
HSDP31	0.7921	0.7955	0.7964	0.7967	0.7969
HSCo300	0.7957	0.7972	0.7975	0.7976	0.7976
HSCo310	0.7937	0.7964	0.7970	0.7972	0.7973
HSCo321	0.7921	0.7955	0.7964	0.7967	0.7969
HSCoSKA3100	0.8018	0.8008	0.7686	0.7363	0.7069
HSCoSKA3101	0.7947	0.7970	0.7578	0.7975	0.7677
HSCoSKA3210	0.7972	0.7987	0.7986	0.7984	0.7168
HSCoSKA3211	0.7933	0.7959	0.7965	0.7969	0.7970
HSCoSKA3000	0.7403	0.7204	0.7006	0.7883	0.6866
HSCoSKA3001	0.7948	0.7970	0.7974	0.7976	0.7678
HSCoA310000	0.7967	0.7976	0.7978	0.7978	0.7978
HSCoA310100	0.7957	0.7972	0.7974	0.7975	0.7976
HSCoA321000	0.7939	0.7965	0.7970	0.7972	0.7973
HSCoA300000	0.7972	0.7977	0.7994	0.7777	0.7688
HSCoA300100	0.7958	0.7972	0.7975	0.7976	0.7976
HSCoA321100	0.7934	0.7962	0.7968	0.7970	0.7971
HSCoCoA310000	0.7967	0.7976	0.7978	0.7978	0.7978
HSCoCoA310100	0.7957	0.7972	0.7974	0.7975	0.7976
HSCoCoA321000	0.7939	0.7965	0.7970	0.7972	0.7973
HSCoCoA300000	0.7972	0.7977	0.7979	0.7777	0.7688
HSCoCoA300100	0.7958	0.7972	0.7975	0.7976	0.7976
HSCoCoA321100	0.7934	0.7962	0.7968	0.7970	0.7971

Table 2: Convergence of the y-coordinate on point A for the parameters shown in Figure 2 and $\mathbf{a}_0^T = [1\ 1\ 1]$.

Figure 6 demonstrat the deformed configurations of some elements together with the v. Mises equivalent stress σ_{VM}. First you can see the bad convergence of the displacement of the H1 and HDP10 element. The over elements shows the typical asymmetric bending caused by the fiber direction much better. Furthermore, all elements show the typical stress distribution for bending (tensile and compressive stress, neutral fibre). Only on the Dirichlet boundary the linear elements show a different stress distribution.

In Figure 7 an element selection is displayed over the computational time (t_{CPU}) for convergence of y-coordinate and the stress σ_{xx}. The high convergence rate of the CoCoA element reduce the computational time at least one order of magnitude.

At least we check the conversation properties on the example of the HSCoCoA210000 element. As expected for a Galerkin time integrator with Gaussian quadrature, the momentum ($\boldsymbol{P}$) and the angular momentum ($\boldsymbol{L}$) are preserved. But for the energy (E) we get an hugh error at the end of simulation. This is because we do not use an energy-momentum scheme to preserve the energy balance.

4 CONCLUTIONS

Our proposed CoCoA element shows the best convergence rate and can reduce the computational time enormously, because coarse meshes are sufficient for accurate solutions in space. Thus, the calculation time and memory requirements with higher polynomial degrees in time is also reduced. We will check these advantages on other example meshes, boundary conditions and material models. Also we will check if the problems of the CoSKA element only appear on this combination of boundary conditions and strain en-

ergy functions. For long-term simulations the hugh energy error is a strong problem. Therefore, in the next step, we extend this element formulations to an energy conserving time integration.

REFERENCES

[1] Simo, J., Taylor, R., Pister., K., 1985. Variational and projection methods for the volume constraint in finite deformation elasto-plasticity. Computer Methods in Applied Mechanics and Engineering 1:177-208.

[2] Simo J.C., Tarnow N., 1992, The discrete energymomentum method. Conserving algorithms for nonlinear elastodynamics. Z. Angew. Math. Phys. (ZAMP), 43:757–792.

[3] Betsch, P., Steinmann., P., 2002. Conservation properties of a time FE methodpart III: Mechanical systems with holonomic constraints. International Journal for Numerical Methods in Engineering 53:2271–2304.

[4] Schröder, J., Wriggers, P., Balzani, D., 2011. A new mixed finite element based on different approximations of the minors of deformation tensors. Computer Methods in Applied Mechanics and Engineering 49:3583–3600.

[5] Erler N. and Groß M., 2015. Energy-momentum conserving higher-order time integration of nonlinear dynamics of finite elastic fiber-reinforced continua. Computational Mechanics 55:921–942.

[6] Schröder, J., Viebahn, V., Wriggers, P., Balzani, D., 2016. A novel mixed finite element for finite anisotropic elasticity; the SKA-element Simplified Kinematics for Anisotropy. Computer Methods in Applied Mechanics and Engineering 310:475–494.

[7] Bartelt, M., Dietzsch., J., Groß., M., 2018. Efficient implementation of energy conservation for higher order finite elements with variational integrators. Mathematics and Computers in Simulation, in press, DOI 10.1016/j.matcom.2018.03.0.

[8] Armero, F., 2008. Assumed strain finite element methods for conserving temporal integrations in nonlinear solid dynamics. International Journal for Numerical Methods in Engineering 74:1795–1847.

[9] Betsch, P., Janz, A., Hesch, C., 2018, A mixed variational framework for the design of energy-momentum schemes inspired by the structure of polyconvex stored energy functions. Computer Methods in Applied Mechanics and Engineering, in press, DOI 10.1016/j.cma.2018.01.013.

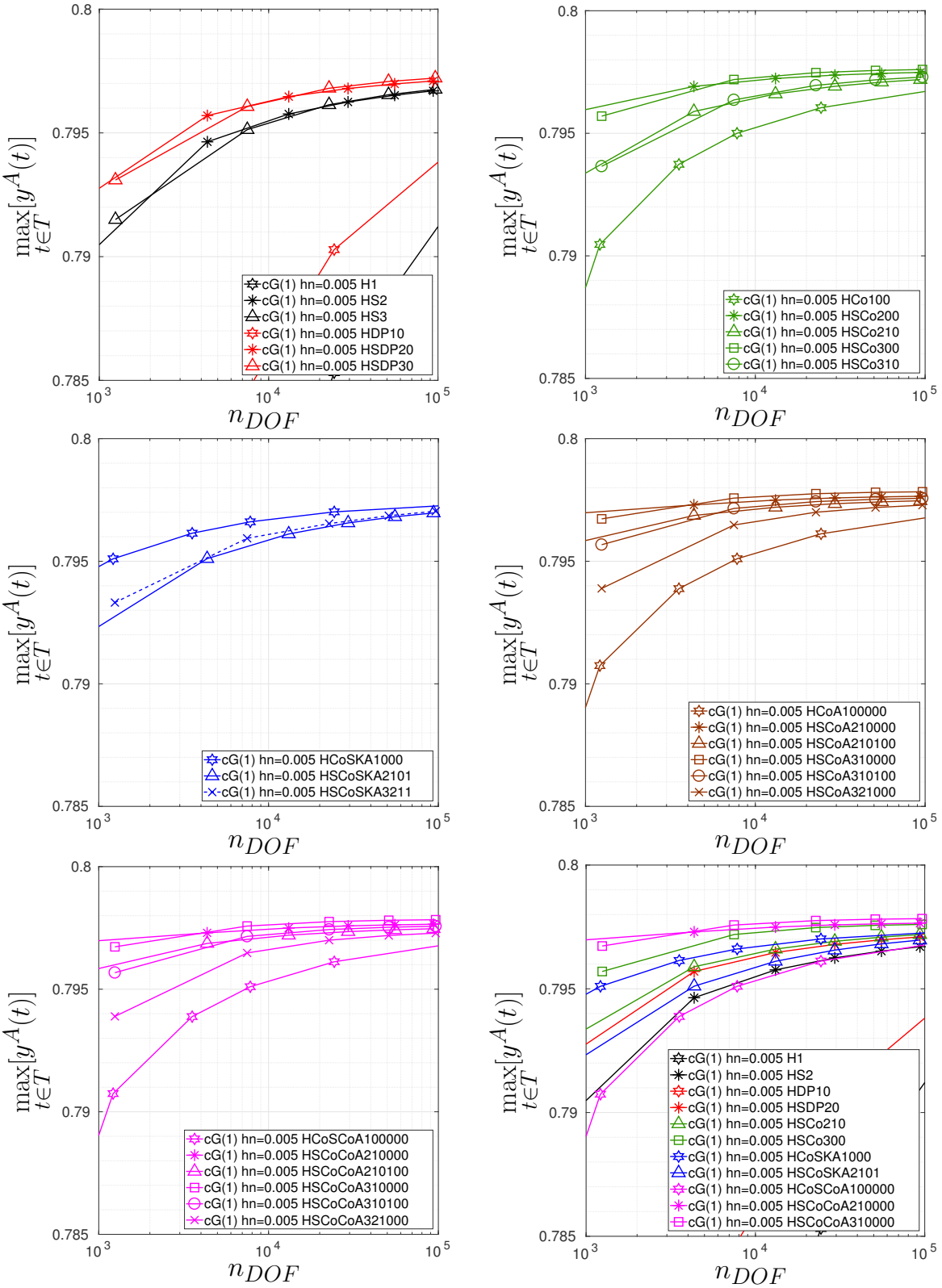

Figure 3: Convergence of the y-coordinate on point A for the parameters shown in Figure 2 and $\mathbf{a}_0^T = [1\ 1\ 1]$.

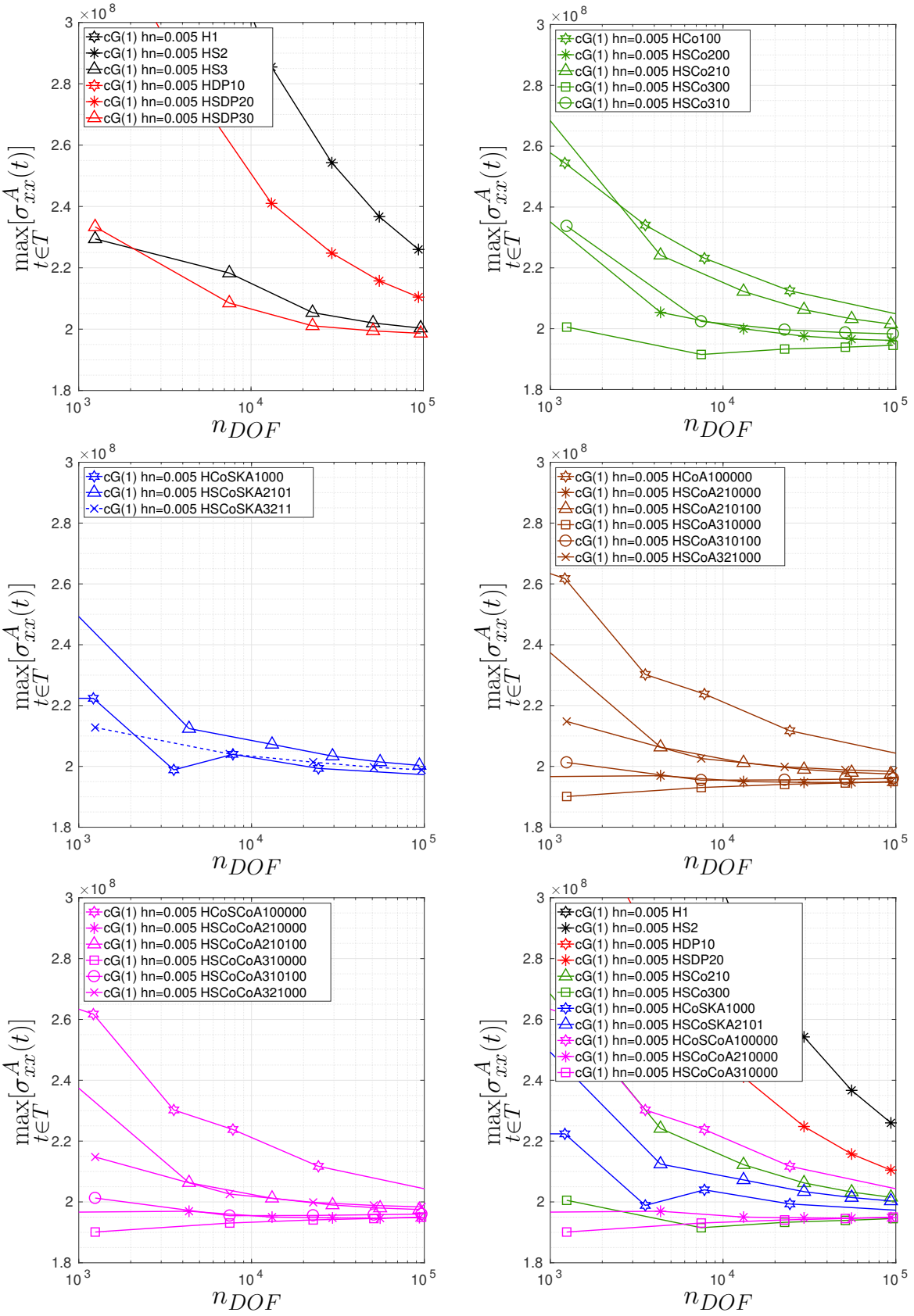

Figure 4: Convergence of σ_{xx} stress on point B for the parameters shown in Figure 2 and $\mathbf{a}_0^T = [1\ 1\ 1]$.

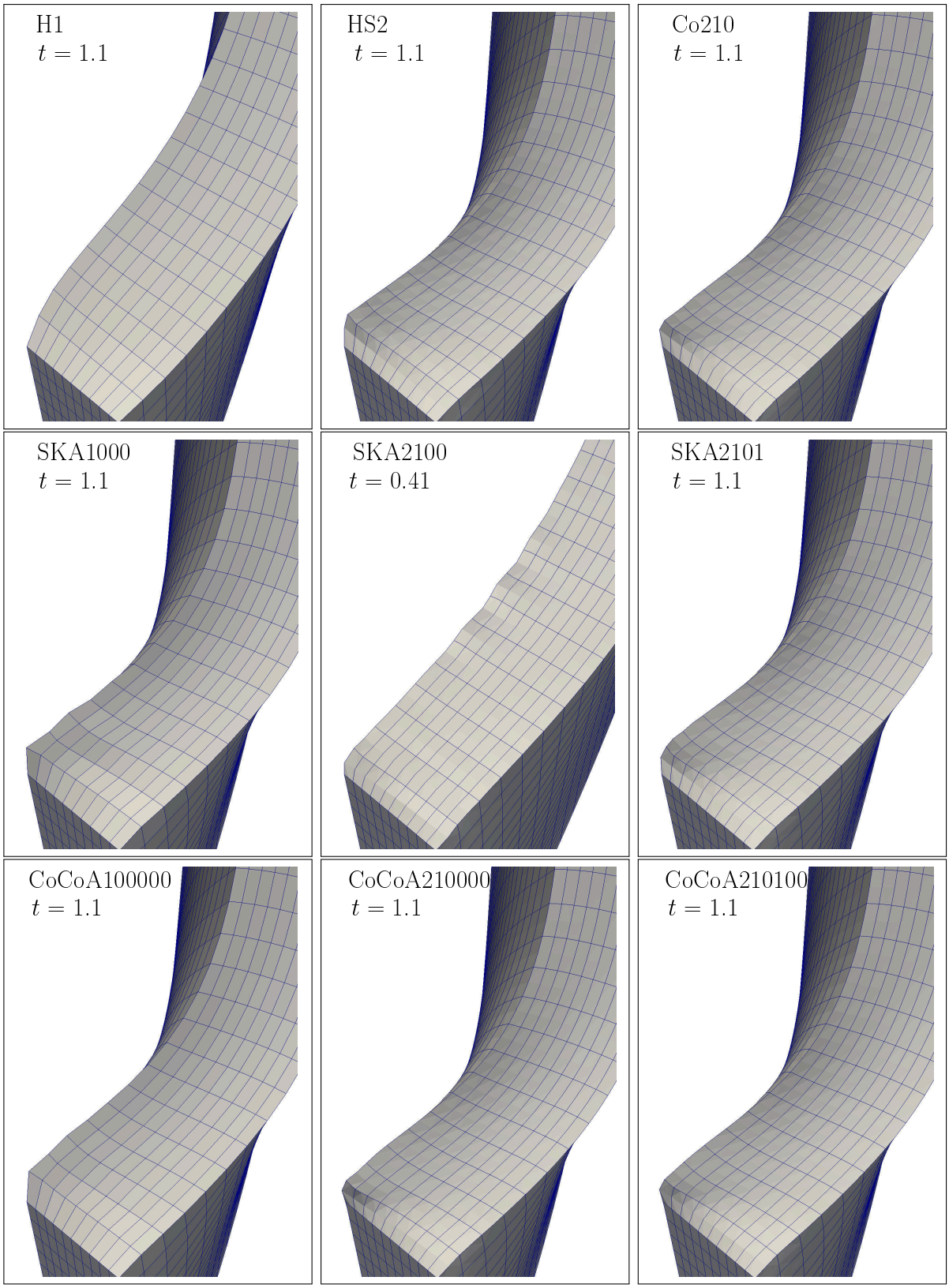

Figure 5: Deformed configuration $\mathcal{B}_t$ for the parameters shown in Figure 2 and $\mathbf{a}_0^T = [1\ 1\ 1]$ for $n_{el} = 4000$.

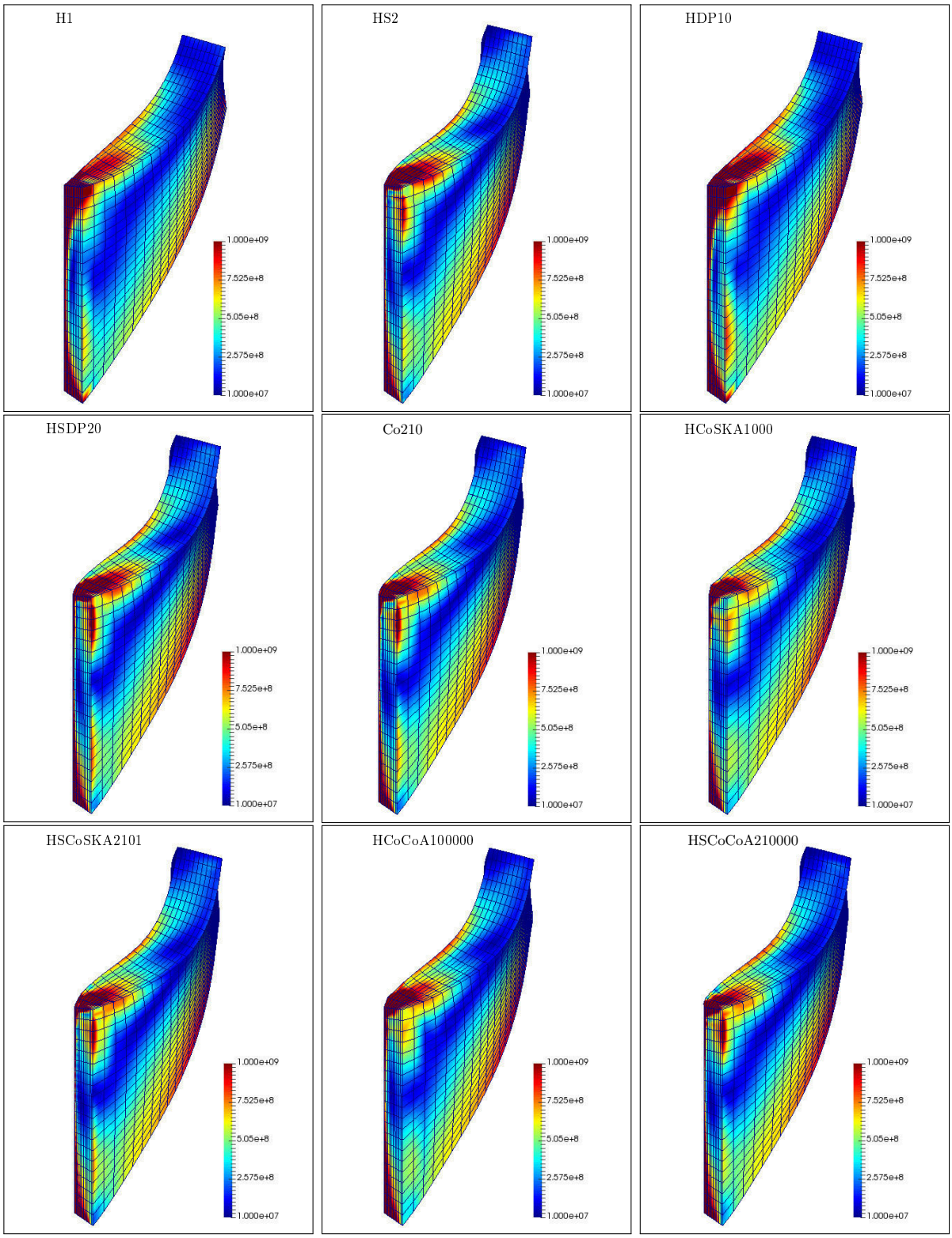

Figure 6: Deformed configuration $\mathcal{B}_t$ and v. Mises equivalent stress σ_{VM} for the parameters shown in Figure 2 and $\mathbf{a}_0^T = [1\ 1\ 1]$ for $n_{el} = 4000$ and $t = 1.1$.

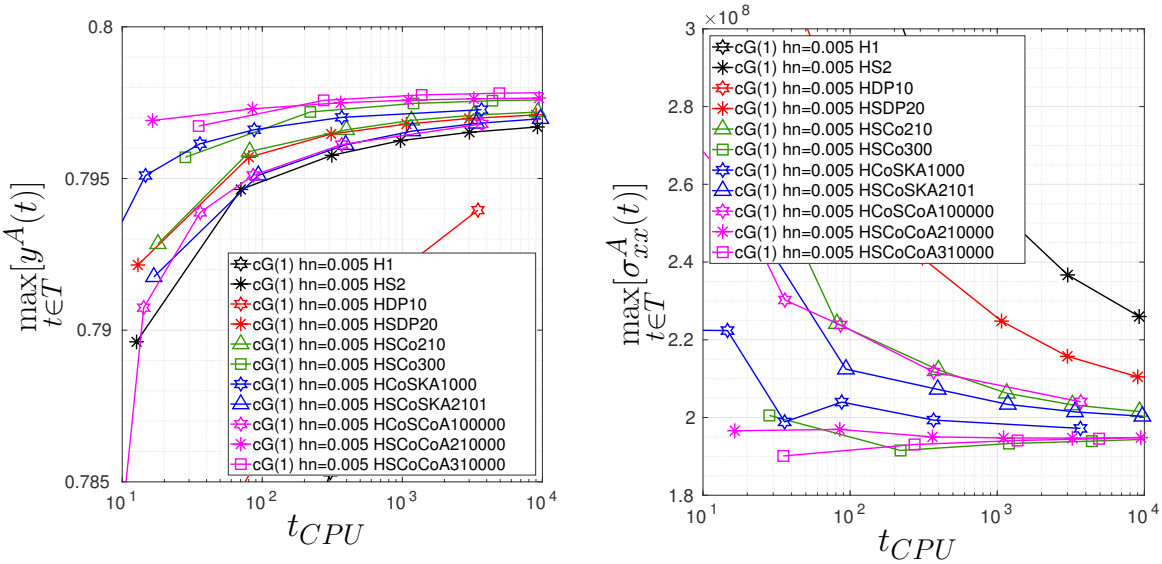

Figure 7: Convergence of the y-coordinate on point A and σ_{xx} stress on point B for the parameters shown in Figure 2 and $\mathbf{a}_0^T = [1\ 1\ 1]$ over calculation time.

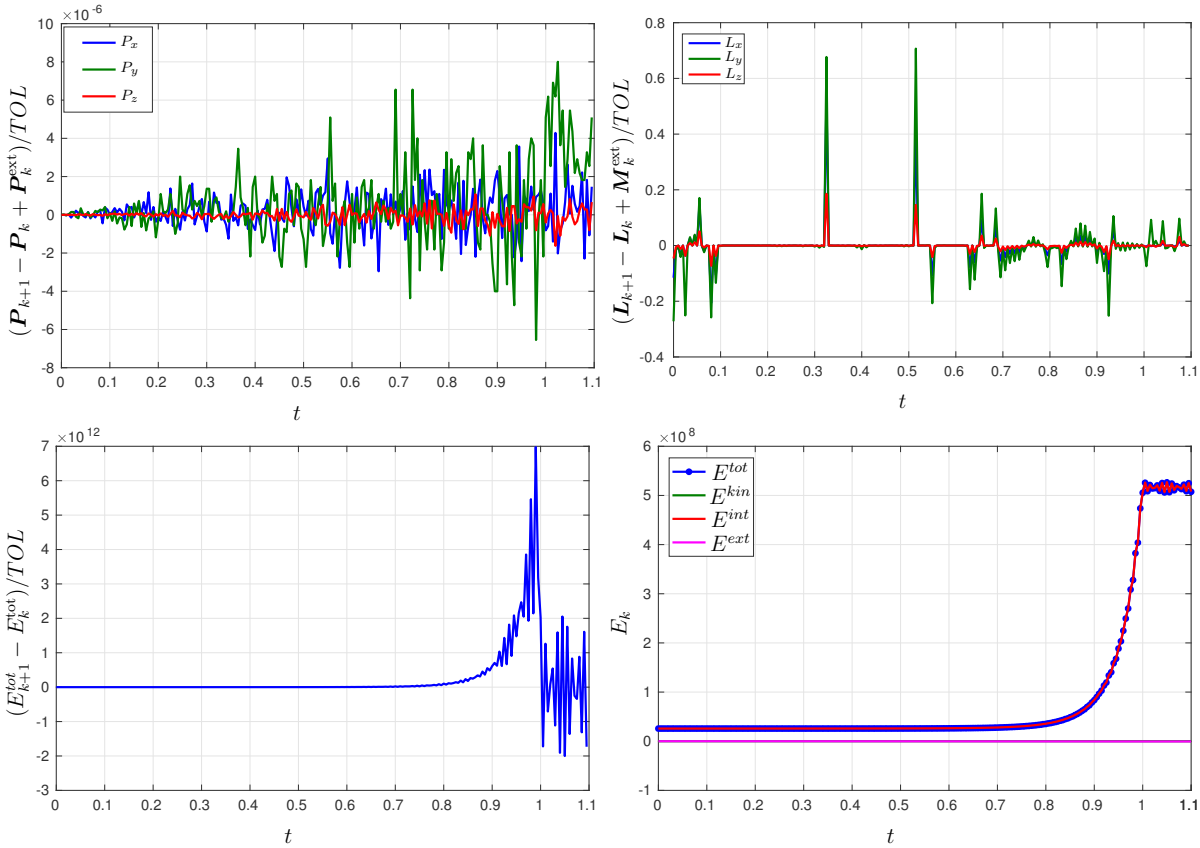

Figure 8: Conversation properties of the HSCoCoA210000 element for the parameters shown in Figure 2 and $\mathbf{a}_0^T = [1\ 1\ 1]$ for $n_{el} = 4000$.